Tran Quang HUNG,[1] Tran Minh TU [iD],[2] Do Minh DUC[1]

Free vibration analysis of sandwich beam with porous FGM core in thermal environment using mesh-free approach

Thermally induced free vibration of sandwich beams with porous functionally graded material core embedded between two isotropic face sheets is investigated in this paper. The core, in which the porosity phase is evenly or unevenly distributed, has mechanical properties varying continuously along with the thickness according to the power-law distribution. Effects of shear deformation on the vibration behavior are taken into account based on both third-order and quasi-3D beam theories. Three typical temperature distributions, which are uniform, linear, and nonlinear temperature rises, are supposed. A mesh-free approach based on point interpolation technique and polynomial basis is utilized to solve the governing equations of motion. Examples for specific cases are given, and their results are compared with predictions available in the literature to validate the approach. Comprehensive studies are carried out to examine the effects of the beam theories, porosity distributions, porosity volume fraction, temperature rises, temperature change, span-to-height ratio, different boundary conditions, layer thickness ratio, volume fraction index on the vibration characteristics of the beam.

1. Introduction

Functionally graded materials (FGMs) are novel composites mixed from materials with different properties. FGMs have a smooth change in physical and mechanical properties. Thus, unlike conventional laminated composite, the stress concentration phenomenon could be eliminated in FGM structures. Typically, FGMs

✉ Tran Minh Tu, e-mail: tutm@nuce.edu.vn

[1]Faculty of Civil Engineering, The University of Da Nang – University of Science and Technology, Da Nang, Vietnam

[2]Hanoi University of Civil Engineering, Hanoi, Vietnam, ORCID: 0000-0002-2208-3463

are often composed of ceramic and metal to promote the high strength of metal and the thermal resistance of ceramic. Thanks to those advantages, FGMs are excellent materials selected for structures working in a high-temperature environment and have a great potential application in areas of nuclear reactor structures, aerospace, solar energy generators, thermal barrier systems, heat exchangers, etc. [1, 2]. Therefore, a deep understanding of the thermal behavior of FGM structural components is particularly important for the design and construction of FGM structures. There have been several studies in the literature conducted by authors [3–19] to examine the mechanical characteristics of FGM beams subjected to thermal loadings. Various computational methods and beam models were employed or proposed to deal with mechanical problems in these studies.

It is shown that during the process of sintering action, micro-voids or porosities could be generated inside FGMs due to the large difference in the solidification temperatures between ceramic and metal components [20–22]. FGMs with porosities could enhance beneficial properties, e.g., sound insulation, thermal resistance, energy absorption, weight reduction. FGM structures containing porosities inside, namely porous FGM (P-FGM) structures in this paper, therefore, become more and more attractive for engineering applications under dynamic loads including thermal effect. In the literature, analyzing behavior of P-FGM beams working in a thermal environment has received great attention from researchers.

Using a refined higher-order shear deformation theory and Navier-type analytical solution, Ibnorachid et al. [23] studied the free vibrations of P-FGM beams resting on Pasternak foundation and exposed to three types of temperature field: uniform, linear, and sinusoidal distributions. Akbas [24] investigated thermal effects on free vibration of P-FGM deep beams. In this study, a plane piecewise solid continua model, and finite element method (FEM) have been used. Babaei et al. [25] performed the thermal buckling and post-buckling of geometrically imperfect P-FGM beams considering third-order shear deformable beam theory (TBT) and physical neutral plane theories by a two-step perturbation method. The thermomechanical vibration characteristics of FGM beams made of porous material subjected to various thermal loadings were investigated by Ebrahimi and Jafari [26] by employing Navier solution and TBT. Liu et al. [27] investigated thermal-mechanical coupling buckling of a clamped-clamped P-FGM sandwich beam based on the physical neutral plane employing high-order sinusoidal shear deformation theory and analytical solution. Mirjavadi et al. [28] presented a study on the thermal buckling behavior of two-dimensional imperfect FGM microscale-tapered porous beams within the framework of classical beam theory and based on the generalized differential quadrature method. Based on the nonlocal elasticity theory, Timoshenko beam model and the Chebyshev-based Ritz procedure, Salari et al. [29] analyzed the nonlinear behavior of thermally preloaded graded porous nanobeams. Ziane et al. [30] predicted the thermal buckling of P-FGM box beams by analytical method and Euler–Bernoulli hypotheses. Aria et al. [31] proposed a nonlocal Timoshenko finite element model to study the thermo-elastic

buckling and vibration behavior of P-FGM nanobeams embedded in the Pasternak foundation.

In the field of numerical analysis, the mesh-free method could be an effective selection in finding approximate solutions for partial differential equations that govern physical phenomena. In the family of mesh-free methods, the one based on point interpolation technique and polynomial basis, proposed by Liu and Gu [32] and shorten here as PIM mesh-fee method, possesses a series of good properties which others desire, e.g., polynomial form and no shape parameters of basis functions that are very efficient for calculation; weight functions are not required to construct shape functions; the constructed shape functions satisfy the Kronecker delta property which is very convenient for imposing essential boundary conditions. PIM mesh-fee method-based one-dimensional (1D) modelling for isotropic beam in conjunction with Euler–Bernoulli theory was first proposed by Gu and Liu [33]. It has recently been developed for FGM sandwich beam with foam core based on TBT by Chinh et al. [34].

According to the literature review, the research on behavior of P-FGM beams in the thermal environment is quite limited when compared to that of solid FGM ones, especially for the thermal vibration responses of sandwich beam with P-FGM core. Besides, no studies have investigated the thermal-stretching effect of quasi-3D theory coupling on behavior of P-FGM beams. Furthermore, there have not been any studies on the vibration analysis of beams for 1D modelling with the framework of quasi-3D theory employing the PIM mesh-fee method yet. Inspired by those facts, this study affords to analyze free vibration of sandwich beams with P-FGM core connected to two solid homogeneous face sheets and placing in thermal environment. Mechanical properties of the core vary smoothly along the thickness according to the power-law variation, and the porosities inside it are assumed to have either even or uneven distribution. Both TBT and quasi-3D beam theories taking into consideration the shear deformation effects on the thermal vibration behavior of the beams are considered. Three types of temperature distribution through the thickness of the beams are supposed: uniform, linear, and nonlinear temperature rises. PIM mesh-free approach is adopted to approximate the displacement field of the problem and discretize the governing equations of motion. Examples for specific cases are presented and their results are compared with those available in the literature to confirm the accuracy. Comprehensive studies are carried out to examine the effects of key parameters on the vibration characteristics of the beams.

2. Theoretical formulations

2.1. Sandwich beam with P-FGM core and material properties

Consider a uniform sandwich beam of length L, width b, and thickness h, placed in the Cartesian coordinate system as shown in Fig. 1. The top and bottom surfaces are, respectively, located at $z = \pm h/2$, and the x-axis is coincided with the

mid-plane. In this paper, two types of FGM due to the distribution of porosities are considered. They are denoted here as Type A and Type B.
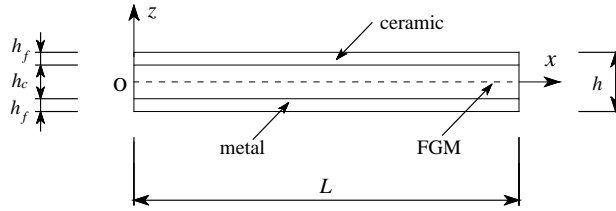
(a) Geometry of a sandwich beam with P-FGM core
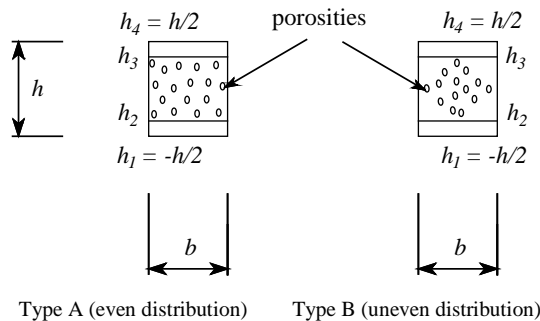
(b) Cross-section with even and uneven porosities

Fig. 1. Uniform sandwich beam

2.1.1. Type A: the pores distribute uniformly (even distribution)

The material properties of the face sheets are constant, whereas those of the core layer vary along the z-axis according to the power-law form as [27]

$$
P(z) = \begin{cases}
P_c, & z \in [h_3, h_4], \\
(P_c - P_m)\left(\dfrac{z - h_2}{h_3 - h_2}\right)^k + P_m - \dfrac{\beta}{2}(P_m + P_c), & z \in [h_2, h_3], \\
P_m, & z \in [h_1, h_2].
\end{cases}
\tag{1}
$$

2.1.2. Type B: the pores distribute around the mid-zone (uneven distribution)

For this FGM type, the expression of material property distribution in Eq. (1) is modified as [27]

$$P(z) = \begin{cases} P_c, & z \in [h_3, h_4], \\ (P_c - P_m) \left(\dfrac{z - h_2}{h_3 - h_2} \right)^k + P_m - \dfrac{\beta}{2} (P_m + P_c) \left(1 - \dfrac{2|z|}{h_3 - h_2} \right), & z \in [h_2, h_3] \\ P_m, & z \in [h_1, h_2]. \end{cases} \quad (2)$$

In Eqs. (1) and (2), m and c represent metal and ceramic, respectively; P stands for material properties, i.e., Young's modulus $E(z)$, thermal conductivity $\kappa(z)$, Poisson's ratio $\nu(z)$, thermal expansion coefficient $\alpha(z)$, and mass density $\rho(z)$; k is the material volume fraction index $(0 \leqslant k)$; β denotes the porosity coefficient which implies the porosity volume fraction over the total volume $(0 \leqslant \beta \ll 1)$.

For materials in thermal environment, the thermo-elastic material properties P_c and P_m (c and m denote ceramic and metal, respectively), which are temperature-dependent, are assumed to follow the nonlinear function of temperature T (in K) as [36]:

$$P_{c/m}(T) = P_0 \left(P_{-1} T^{-1} + 1 + P_1 T^1 + P_2 T^2 + P_3 T^3 \right), \quad (3)$$

where P_0, P_{-1}, P_1, P_2, and P_3 are the temperature-dependent coefficients and are unique to each constituent material, which are listed in Table 1 for Si_3N_4 (representing ceramic) and SUS304 (representing metal).

Table 1. Temperature-dependent coefficients of materials [9, 35]

Properties	P_0	P_{-1}	P_1	P_2	P_3
Si_3N_4 (Silicon nitride)					
E (Pa)	348.43e+9	0	−3.070e−4	2.160e−7	−8.946e−11
α (K^{-1})	5.8723e−6	0	9.095e−4	0	0
ρ (kg/m^3)	2370	0	0	0	0
κ (W/mK)	13.723	0	−1.032e−3	5.466e−7	−7.876e−11
ν	0.24	0	0	0	0
SUS304 (Stainless steel)					
E (Pa)	201.04e+9	0	3.079e−4	−6.534e−7	0
α (K^{-1})	12.330e−6	0	8.086e−4	0	0
ρ (kg/m^3)	8166	0	0	0	0
κ (W/mK)	15.379	0	−1.246e−3	2.092e−6	−7.223e−10
ν	0.3262	0	−2.002e−4	3.797e−7	0

Fig. 2 demonstrates the variations of Young's modulus $E(z)$ through the thickness of the beam with different values of porosity coefficient β. Material properties are taken from Table 1. It is seen that increasing β results in a reduction in $E(z)$ of the porous core and an increase in the discontinuity of $E(z)$ at the interface layers (Fig. 2a). This discontinuity sometimes causes the delamination. However, it is assumed in this study that the faces are perfectly bonded to the core. In other words,

the displacement of the beam between the layers is supposed to be continuous. It should be noted that in contrast to Type A, $E(z)$ of Type B is continuous, which is shown in Fig. 2b.

(a) Type A (even distribution)   (b) Type B (uneven distribution)
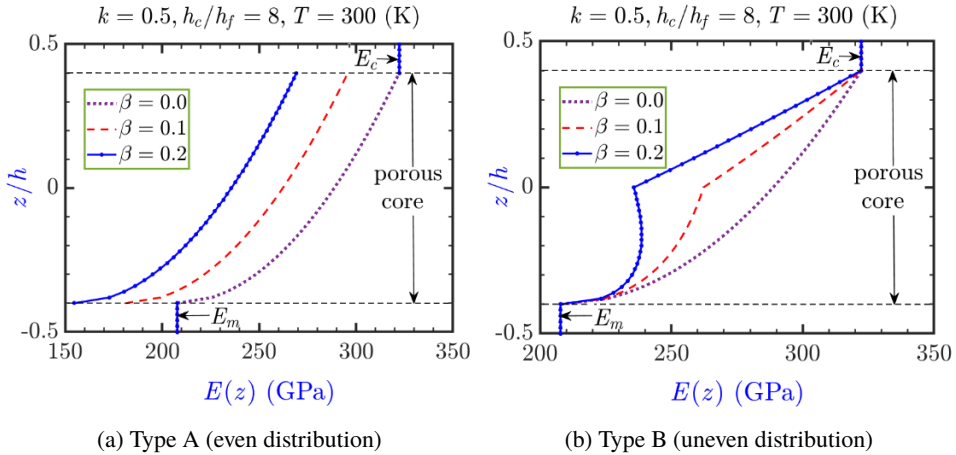
Fig. 2. Through-the-thickness distribution of Young's modulus $E(z)$ according to Eqs. (1) and (2)

2.2. Temperature distributions

2.2.1. Uniform temperature rise (UTR)

The current temperature T in the whole domain of the beam is changed ΔT from the initial temperature T_0. Hence, its expression can be written as

$$T(z) = T_0 + \Delta T. \tag{4}$$

2.2.2. Linear temperature rise (LTR)

The temperature field in the beam varies linearly along with the thickness and could be expressed as

$$T(z) = T_L + (T_U - T_L)\left(\frac{z}{h} + \frac{1}{2}\right), \tag{5}$$

where T_U and T_L are current temperatures at the top and bottom surfaces of the beam, respectively.

2.2.3. Nonlinear temperature rise (NTR)

For this case, the temperature field in the beam varies nonlinearly along with the thickness and could be determined from the 1D steady-state heat conduction:

$$-\frac{\mathrm{d}}{\mathrm{d}z}\left(\kappa^{(i)}(z)\frac{\mathrm{d}T(z)}{\mathrm{d}z}\right) = 0. \tag{6}$$

Based on thermal continuous conditions between two adjacent layers, the solution of Eq. (6) is obtained in the following form [16]

$$T^{(i)}(z) = (T_U - T_L) \frac{\Theta^{(i)}}{\Sigma K} + T_L,$$ (7)

where

$$
\Theta^{(1)} = \int\limits_{h_1}^{z} \frac{1}{\kappa^{(1)}(z)} \, dz, \qquad\qquad\qquad z \in [h_1, h_2],
$$

$$
\Theta^{(2)} = \int\limits_{h_1}^{h_2} \frac{1}{\kappa^{(1)}(z)} \, dz + \int\limits_{h_2}^{z} \frac{1}{\kappa^{(2)}(z)} \, dz, \qquad\qquad z \in [h_2, h_3],
$$

$$
\Theta^{(3)} = \int\limits_{h_1}^{h_2} \frac{1}{\kappa^{(1)}(z)} \, dz + \int\limits_{h_2}^{h_3} \frac{1}{\kappa^{(2)}(z)} \, dz + \int\limits_{h_3}^{z} \frac{1}{\kappa^{(3)}(z)} \, dz, \quad z \in [h_3, h_4],
$$

$$
\Sigma K = \int\limits_{h_1}^{h_2} \frac{1}{\kappa^{(1)}(z)} \, dz + \int\limits_{h_2}^{h_3} \frac{1}{\kappa^{(2)}(z)} \, dz + \int\limits_{h_3}^{h_4} \frac{1}{\kappa^{(3)}(z)} \, dz,
$$

(8)

and T_U and T_L are current temperatures at the top and bottom surfaces of the beam, respectively; κ is the thermal conductivity coefficient; the superscript i ($i = 1, 2, 3$) denotes the i-th layer.

In this study, it is assumed that the mechanical properties of the bottom and the top isotropic layers are evaluated at the temperature T_L and T_U, respectively.

2.3. The displacement, strain, and stress fields

Based on the quasi-3D shear deformation theory, which includes both the shear deformation and thickness stretching effects, the displacement field in the beam could be described in compact form as [2, 37].

$$
\mathbf{d} = \begin{Bmatrix} u \\ w \end{Bmatrix} = \underbrace{\begin{bmatrix} 1 & 0 & -z & \Phi(z) & 0 \\ 0 & 1 & 0 & 0 & \dfrac{\partial \Phi(z)}{\partial z} \end{bmatrix}}_{\Phi_1} \mathbf{A}_1 = \mathbf{\Phi}_1 \mathbf{A}_1,
$$ (9)

$$
\mathbf{A}_1^{\mathrm{T}} = \left\{ u_o(x,t) \quad w_o(x,t) \quad \frac{\partial w_o(x,t)}{\partial x} \quad \varphi_{os}(x,t) \quad w_{oz}(x,t) \right\},
$$ (10)

in which u_o, w_o, φ_{os} and w_{oz} are the four unknown displacement functions of any point on the mid-plane; $\Phi(z)$ is the shape function which characterizes the shear

strain distribution over the cross-section. In this work, the third-order function $\Phi(z) = z - 4z^3/(3h^2)$ [38] is used; the exponent $(\cdot)^{\mathrm{T}}$ indicates the transpose of a matrix; t denotes the time. It should be noted that the third-order beam theory (TBT) is restored if the thickness stretching effect is omitted ($w_{oz} = 0$).

The strain field associated with the displacement field in Eq. (9) is expressed as follows

$$
\boldsymbol{\varepsilon} = \begin{Bmatrix} \varepsilon_x \\ \varepsilon_z \\ \gamma_{xz} \end{Bmatrix} = \underbrace{\begin{bmatrix} 1 & -z & \Phi(z) & 0 & 0 & 0 \\ 0 & 0 & 0 & \dfrac{\partial^2 \Phi(z)}{\partial z^2} & 0 & 0 \\ 0 & 0 & 0 & 0 & \dfrac{\partial \Phi(z)}{\partial z} & \dfrac{\partial \Phi(z)}{\partial z} \end{bmatrix}}_{\boldsymbol{\Phi}_2} \mathbf{A}_2 = \boldsymbol{\Phi}_2 \mathbf{A}_2, \quad (11)
$$

where

$$
\mathbf{A}_2^{\mathrm{T}} = \left\{ \frac{\partial u_o(x,t)}{\partial x} \quad \frac{\partial^2 w_o(x,t)}{\partial x^2} \quad \frac{\partial \varphi_{os}(x,t)}{\partial x} \quad w_{oz}(x,t) \quad \varphi_{os}(x,t) \quad \frac{\partial w_{oz}(x,t)}{\partial x} \right\}.
$$

(12)

The stress-strain relationship obeys Hooke's law and could be presented by matrix form below for the plan stress condition.

$$
\boldsymbol{\sigma} = \begin{Bmatrix} \sigma_x \\ \sigma_z \\ \tau_{xz} \end{Bmatrix} = \underbrace{\begin{bmatrix} Q_{11} & Q_{12} & 0 \\ Q_{21} & Q_{22} & 0 \\ 0 & 0 & Q_{33} \end{bmatrix}}_{\mathbf{E}_d} \left(\begin{Bmatrix} \varepsilon_x \\ \varepsilon_z \\ \gamma_{xz} \end{Bmatrix} - \underbrace{\begin{Bmatrix} \alpha(T - T_0) \\ \alpha(T - T_0) \\ 0 \end{Bmatrix}}_{\boldsymbol{\varepsilon}^{th}} \right) = \mathbf{E}_d \left(\boldsymbol{\varepsilon} - \boldsymbol{\varepsilon}^{th} \right), \quad (13)
$$

where

$$
Q_{11} = Q_{22} = \frac{E(z)}{[1 - \nu(z)^2]}, \qquad Q_{12} = Q_{21} = \nu(z)Q_{11},
$$

$$
Q_{33} = G(z) = \frac{E(z)}{2\,[1 + \nu(z)]}\,.
$$

(14)

Eq. (13) expresses the stress-strain relationship for quasi-3D beam theory. However, this equation can be used for TBT by setting $Q_{11} = E(z)$, $Q_{12} = Q_{12} = Q_{22} = 0$.

2.4. Energies in the beam

2.4.1. The internal virtual work done by internal stresses

$$
\delta W^{\mathrm{int}} = \int_V \boldsymbol{\sigma}^{\mathrm{T}} \delta \boldsymbol{\varepsilon} \, \mathrm{d}V. \quad (15)
$$

For free vibration problems, there is no need to consider the virtual work due to thermal stresses participating in Eq. (15) because those stresses play a role of external loads. Hence, ignoring the thermal strain $\boldsymbol{\varepsilon}^{th}$ in Eq. (13) and substituting this equation into Eq. (15), the internal virtual work is rewritten as

$$\delta W^{\text{int}} = \int_V \boldsymbol{\varepsilon}^{\text{T}} \mathbf{E}_d \delta \boldsymbol{\varepsilon} \, \mathrm{d}V. \tag{16}$$

Next, substituting Eq. (11) into Eq. (16), the virtual work is then expressed through the displacements:

$$\delta W^{\text{int}} = \int_0^L \mathbf{A}_2^{\text{T}} \mathbf{D}_E \delta \mathbf{A}_2 \, \mathrm{d}x, \tag{17}$$

where matrix containing stiffnesses is defined as

$$\mathbf{D}_E = b \int_{h_1}^{h_4} \boldsymbol{\Phi}_2^{\text{T}} \mathbf{E}_d \boldsymbol{\Phi}_2 \, \mathrm{d}z. \tag{18}$$

2.4.2. The external virtual work of axial thermal stress resultant

$$\delta W_1^{\text{ext}} = \int_0^L N^{th} \frac{\partial w_o}{\partial x} \frac{\partial \delta w_o}{\partial x} \, \mathrm{d}x, \tag{19}$$

where axial thermal stress resultant is given by

$$N^{th} = -b \int_{h_1}^{h_4} [Q_{11}(z) + Q_{12}(z)] \, \alpha(z) \, [T(z) - T_0] \, \mathrm{d}z$$

$$= -b \int_{h_1}^{h_4} \left(\sigma_{x1}^{th} + \sigma_{x2}^{th} \right) \, \mathrm{d}z, \tag{20}$$

$$\sigma_{x1}^{th} = Q_{11}(z)\alpha(z) \, [T(z) - T_0], \qquad \sigma_{x2}^{th} = Q_{12}(z)\alpha(z) \, [T(z) - T_0], \tag{21}$$

in which σ_{x1}^{th}, σ_{x2}^{th} are the axial stresses due to the thermal strain in the x- and z-directions, respectively.

If TBT is used ($Q_{11} = E(z)$, $Q_{12} = 0$), Eq. (20) is reduced to:

$$N^{th} = -b \int_{h_1}^{h_4} Q_{11}(z)\alpha(z) \, [T(z) - T_0] \, \mathrm{d}z = -b \int_{h_1}^{h_4} E(z)\alpha(z) \, [T(z) - T_0] \, \mathrm{d}z. \tag{22}$$

2.4.3. The external virtual work done due to the inertia forces

$$\delta W_2^{\text{ext}} = \int_V \rho(z)\ddot{\mathbf{d}}^{\text{T}}\delta\mathbf{d}\,\mathrm{d}V. \tag{23}$$

By substituting the displacement vector from Eq. (9) into Eq. (23), the external virtual work becomes:

$$\delta W_2^{\text{ext}} = \int_0^L \ddot{\mathbf{A}}_1^{\text{T}}\mathbf{D}_R\delta\mathbf{A}_1\,\mathrm{d}x, \tag{24}$$

where

$$\mathbf{D}_R = b\int_{h_1}^{h_4} \mathbf{\Phi}_1^{\text{T}}\rho(z)\mathbf{\Phi}_1\,\mathrm{d}z, \tag{25}$$

and the two superscript dots (··) denote the double differentiation to time t.

It is noted that the integration of Eqs. (18), (20), (22) and (25) is a cumulative formulation, i.e., $\int_{h_1}^{h_4} \chi(z)\,\mathrm{d}z = \int_{h_1}^{h_2} \chi(z)\,\mathrm{d}z + \int_{h_2}^{h_3} \chi(z)\,\mathrm{d}z + \int_{h_3}^{h_4} \chi(z)\,\mathrm{d}z$, where $\chi(z)$ is an arbitrary function of z.

2.4.4. Virtual work principle

The beam is in an equilibrium state if the energies satisfy the virtual work principle which is expressed as following mathematical formulation [39].

$$\delta W^{\text{int}} + \delta W^{\text{ext}} = \delta W^{\text{int}} + \delta W_1^{\text{ext}} + \delta W_2^{\text{ext}} = 0. \tag{26}$$

2.5. Mesh-free approach

2.5.1. Displacement field approximation

In the current work, PIM (point interpolation technique based on the polynomial basis) [40] is utilized to obtain the displacement field approximation of the 1D beam modelling. Only key steps of the procedure for constructing the shape functions are presented herein. Detailed explanations could be found in [33, 40].

The problem domain is represented by a set of arbitrarily distributed nodes, also called the field nodes [40], along the x-axis. The four-component displacement field, i.e., u_o, w_o, φ_{os} and w_{oz}, can be approximated through displacements at the nodes in an influence domain Ω_s, which is a sub-domain of the problem domain. In this study, the variable w_o is interpolated using the deflection and slope (Hermite interpolation), while each of the field variables u_o, φ_{os} and w_{oz} is interpolated

using one displacement at each node (Lagrange interpolation). Thus, the shape functions to approximate the variables u_o, φ_{os} and w_{oz} are the same. Therefore, it is necessary to construct the shape functions for w_o and one of the remaining variables, e.g., u_o.

The approximation of u_o and w_o using the polynomial basis can be expressed:

$$
\begin{aligned}
u_o(x,t) &= \sum_{i=1}^{n} p_u^{(i)}(x) a_u^{(i)}(t) = \mathbf{p}_u^{\mathrm{T}}(x) \mathbf{a}_u(t), \\
w_o(x,t) &= \sum_{i=1}^{2n} p_w^{(i)}(x) a_w^{(i)}(t) = \mathbf{p}_w^{\mathrm{T}}(x) \mathbf{a}_w(t)
\end{aligned}
\tag{27}
$$

in which n is equal to the total number of nodes belonging to the influence domain Ω_s; $\mathbf{a}$ and $\mathbf{p}(x)$ are, respectively, the vectors of coefficients and polynomial basis (monomials). These vectors are given by

$$
\begin{aligned}
\mathbf{p}_u^{\mathrm{T}}(x) &= \left\{ 1 \quad x \quad x^2 \quad ... \quad x^{n-1} \right\}, \\
\mathbf{p}_w^{\mathrm{T}}(x) &= \left\{ 1 \quad x \quad x^2 \quad ... \quad x^{2n-1} \right\},
\end{aligned}
\tag{28}
$$

$$
\begin{aligned}
\mathbf{a}_u &= \left\{ a_u^{(1)} \quad a_u^{(2)} \quad ... \quad a_u^{(n)} \right\}^{\mathrm{T}}, \\
\mathbf{a}_w &= \left\{ a_w^{(1)} \quad a_w^{(2)} \quad ... \quad a_w^{(2n)} \right\}^{\mathrm{T}}.
\end{aligned}
\tag{29}
$$

Note that $\mathbf{p}_w^{\mathrm{T}}(x)$ has $2 \times n$ terms because the Hermite interpolation, which requires both transverse and rotational displacements, is used for approximating w_o.

The total $(3 \times n)$ unknown coefficients in the vectors $\mathbf{a}_u$ and $\mathbf{a}_w$ are determined by enforcing Eq. (27) to pass through all the n nodes in the influence domain Ω_s. Assuming that the nodal values of u_o and w_o of the j-th node located at $x = x^{(j)}$ are $\mathbf{q}^{(j)\mathrm{T}} = \left\{ u_o^{(j)} \quad w_o^{(j)} \quad \theta_o^{(j)} \right\}$; where $\theta_o^{(j)} = \partial w_o \left(x^{(j)} \right) / \partial x$. Hence:

$$
\mathbf{q}^{(j)} = \left\{ \begin{matrix} u_o^{(j)} \\ w_o^{(j)} \\ \theta_o^{(j)} \end{matrix} \right\} = \left\{ \begin{matrix} u_o \left(x^{(j)}, t \right) \\ w_o \left(x^{(j)}, t \right) \\ \dfrac{\partial w_o \left(x^{(j)}, t \right)}{\partial x} \end{matrix} \right\} = \left\{ \begin{matrix} \displaystyle\sum_{i=1}^{n} p_u^{(i)} \left(x^{(j)} \right) a_u^{(i)} = \mathbf{p}_u^{\mathrm{T}} \left(x^{(j)} \right) \mathbf{a}_u, \\ \displaystyle\sum_{i=1}^{2n} p_w^{(i)} \left(x^{(j)} \right) a_w^{(i)} = \mathbf{p}_w^{\mathrm{T}} \left(x^{(j)} \right) \mathbf{a}_w, \\ \displaystyle\sum_{i=1}^{2n} \dfrac{\partial p_w^{(i)} \left(x^{(j)} \right)}{\partial x} a_w^{(i)} = \dfrac{\partial \mathbf{p}_w^{\mathrm{T}} \left(x^{(j)} \right)}{\partial x} \mathbf{a}_w. \end{matrix} \right.
\tag{30}
$$

For $j = 1, ..., n$ (repeating for all nodes in the influence domain), Eq. (30) can then be rearranged and written in the matrix form as

$$
\mathbf{q}_{\Omega_s} = \mathbf{P}_{Q(3n \times 3n)} \underbrace{\left\{ \mathbf{a}_u \quad \mathbf{a}_w \right\}^{\mathrm{T}}}_{\mathbf{a}} = \mathbf{P}_{Q(3n \times 3n)} \mathbf{a}_{(3n \times 1)},
\tag{31}
$$

where $\mathbf{P}_Q$ is called the moment matrix [40] given by

$$\mathbf{P}_{Q(3n \times 3n)} = \begin{bmatrix} \mathbf{P}_{Q1} & \mathbf{0} \\ \mathbf{0} & \mathbf{P}_{Q2} \end{bmatrix}, \tag{32}$$

in which

$$\mathbf{P}_{Q1(n \times n)} = \left\{ \mathbf{p}_u^T \left(x^{(1)} \right) \ \ \mathbf{p}_u^T \left(x^{(2)} \right) \ \ \ldots \ \ \mathbf{p}_u^T \left(x^{(n)} \right) \right\}^T, \tag{33}$$

$$\mathbf{P}_{Q2(2n \times 2n)} = \left\{ \mathbf{p}_w^T \left(x^{(1)} \right) \ \frac{\partial \mathbf{p}_w^T \left(x^{(1)} \right)}{\partial x} \ \ \mathbf{p}_w^T \left(x^{(2)} \right) \ \frac{\partial \mathbf{p}_w^T \left(x^{(2)} \right)}{\partial x} \ \ \ldots \right. \\ \left. \ldots \ \mathbf{p}_w^T \left(x^{(n)} \right) \ \ \frac{\partial \mathbf{p}_w^T \left(x^{(n)} \right)}{\partial x} \right\}^T . \tag{34}$$

In Eq. (31), $\mathbf{q}_{\Omega_s}$ is a $3n \times 1$ vector that collects all the nodal displacements of u_o and w_o within the influence domain Ω_s.

$$\mathbf{q}_{\Omega_s} = \{ u_o^{(1)} \ u_o^{(2)} \ \ldots \ u_o^{(n)} \ w_o^{(1)} \ \theta_o^{(1)} \ w_o^{(2)} \ \theta_o^{(2)} \ \ldots \ w_o^{(n)} \ \theta_o^{(n)} \}^T. \tag{35}$$

From Eq. (31), the coefficients of the polynomial approximations are determined by inverting the moment matrix and described as

$$\mathbf{a} = \mathbf{P}_Q^{-1} \mathbf{q}_{\Omega_s} . \tag{36}$$

Note that for 1D point interpolations, matrix $\mathbf{P}_Q^{-1}$ always exists providing that the nodes in the influence domain are not duplicated [40], which is easily guaranteed in practical implementation.

Substituting the coefficients back into Eq. (27), the displacement field is then described through the nodal values $\mathbf{q}_{\Omega_s}$:

$$\begin{Bmatrix} u_o(x,t) \\ w_o(x,t) \end{Bmatrix} = \begin{bmatrix} \mathbf{p}_u^T(x) & \mathbf{0} \\ \mathbf{0} & \mathbf{p}_w^T(x) \end{bmatrix} \mathbf{a} = \underbrace{\begin{bmatrix} \mathbf{p}_u^T(x) & \mathbf{0} \\ \mathbf{0} & \mathbf{p}_w^T(x) \end{bmatrix} \mathbf{P}_Q^{-1}}_{\mathbf{\eta}(x)} \mathbf{q}_{\Omega_s} = \mathbf{\eta}(x)\mathbf{q}_{\Omega_s}, \tag{37}$$

where $\mathbf{\eta}(x)$ is a matrix of PIM shape functions defined by

$$\mathbf{\eta}(x) = \begin{bmatrix} \eta_u^{(1)} & \eta_u^{(2)} & \ldots & \eta_u^{(n)} & 0 & 0 & 0 & 0 & \ldots & 0 & 0 \\ 0 & 0 & \ldots & 0 & \eta_w^{(1)} & \eta_\theta^{(1)} & \eta_w^{(2)} & \eta_\theta^{(2)} & \ldots & \eta_w^{(n)} & \eta_\theta^{(n)} \end{bmatrix}_{(2 \times 3n)}$$

$$= \begin{bmatrix} \mathbf{p}_u^T(x) & \mathbf{0} \\ \mathbf{0} & \mathbf{p}_w^T(x) \end{bmatrix} \mathbf{P}_Q^{-1} . \tag{38}$$

As stated above, the shape functions $\eta_u^{(j)}$ can also be used to approximate the variables φ_{os} and w_{oz}. Rearranging the nodal displacements with groups of node-by-node displacements and the corresponding shape functions, and then substituting them into all the displacement field variables, the approximated displacement functions can be described through the nodal displacements as

$$
\begin{Bmatrix} u_o(x,t) \\ w_o(x,t) \\ \varphi_{os}(x,t) \\ w_{oz}(x,t) \end{Bmatrix} = \begin{bmatrix} \eta_u^{(1)} & 0 & 0 & 0 & 0 & \dots & \eta_u^{(n)} & 0 & 0 & 0 & 0 \\ 0 & \eta_w^{(1)} & \eta_\theta^{(1)} & 0 & 0 & \dots & 0 & \eta_w^{(n)} & \eta_\theta^{(n)} & 0 & 0 \\ 0 & 0 & 0 & \eta_u^{(1)} & 0 & \dots & 0 & 0 & 0 & \eta_u^{(n)} & 0 \\ 0 & 0 & 0 & 0 & \eta_u^{(1)} & \dots & 0 & 0 & 0 & 0 & \eta_u^{(n)} \end{bmatrix} \mathbf{q}_{\Omega_s}, \quad (39)
$$

where the nodal displacement vector $\mathbf{q}_{\Omega_s}$ is now redefined and given as

$$
\mathbf{q}_{\Omega_s} = \begin{Bmatrix} u_o^{(1)} & w_o^{(1)} & \theta_o^{(1)} & \varphi_o^{(1)} & w_{oz}^{(1)} & u_o^{(2)} & w_o^{(2)} & \theta_o^{(2)} & \varphi_o^{(2)} & w_{oz}^{(2)} & \dots \\ & & & & \dots & u_o^{(n)} & w_o^{(n)} & \theta_o^{(n)} & \varphi_o^{(n)} & w_{oz}^{(n)} \end{Bmatrix}^{\mathrm{T}}. \quad (40)
$$

In Eq. (40), $\varphi_o^{(j)}$ and $w_{oz}^{(j)}$ are the nodal displacements at the j-th node. They correspond to the displacements φ_{os} and w_{oz}, respectively.

The characteristics (e.g., number of nodes, nodal distribution, node coordinates, size) of different influence domains are not the same. Therefore, in general, the shape functions need to be reconstructed when a new influence domain is considered. Consequently, the approximated displacement field must be rebuilt for each of the influence domains.

2.5.2. Discrete system equations

Based on the mesh-free concepts, the physical domain of the beam is divided into a set of non-overlapping sub-domains Ω_q, called the background cells, which are independent of nodes and influence domains. Because each background cell (e.g., Ω_q) belongs to an influence domain (e.g., Ω_s), the displacement field in the background cell Ω_q is also the displacement field in the influence domain Ω_s which is approximated by Eq. (39). Therefore, substituting Eq. (39) into the energy expressions, Eqs. (17), (19) and (24), the energies are expressed through the nodal displacements $\mathbf{q}_{\Omega_s}$. Next, applying the virtual work principle, Eq. (26), one obtains the algebraic equations expressing the equilibrium of forces in the domain Ω_q. This procedure is similar to the conventional FEM. For free vibration, these equations could be written in the matrix form as

$$
\mathbf{M}_{\Omega_q} \ddot{\mathbf{q}}_{\Omega s} + \left(\mathbf{K}_{\Omega q} + \mathbf{K}_{\Omega q}^G \right) \mathbf{q}_{\Omega s} = \{\mathbf{0}\}, \quad (41)
$$

where $\mathbf{M}_{\Omega_q}$ is the mass matrix, $\mathbf{K}_{\Omega_q}$ is the elastic stiffness matrix, $\mathbf{K}_{\Omega_q}^G$ is the geometric stiffness matrix due to the thermal loadings.

It should be noted that the energy expressions and the principle of virtual work in subsection 2.4.4 are expressed for the whole domain of the beam. However, they can be applied for the sub-domain Ω_q of the problem to derive Eq. (41).

For all background cells, Eq. (41) is subsequently assembled into the system of global discrete equations:

$$\mathbf{M\ddot{q}} + \left(\mathbf{K} + \mathbf{K}^G\right)\mathbf{q} = \{\mathbf{0}\}, \tag{42}$$

where $\mathbf{M}$ is the global mass matrix; $\mathbf{K}$ and $\mathbf{K}^G$ are the global elastic and geometric stiffness matrices, respectively; $\mathbf{q}$ is the nodal displacement vector for the whole domain of the beam; $\{\mathbf{0}\}$ is the null vector.

For free vibration analysis, the displacement functions are assumed as harmonic functions below

$$\mathbf{q} = \mathbf{\Delta}e^{i\omega t}, \tag{43}$$

where ω is the natural frequency of the beam, and $i = \sqrt{-1}$ is the unit imaginary number; $\mathbf{\Delta}$ is a vector collecting the nodal values corresponding to the amplitudes of the displacements.

Substituting Eq. (43) into Eq. (42) leads to the frequency equations which can be expressed as

$$\left(\mathbf{K} + \mathbf{K}^G - \omega^2\mathbf{M}\right)\mathbf{\Delta} = \{\mathbf{0}\}. \tag{44}$$

To ensure the compatibility of PIM automatically, so that the virtual work principle (a type of global energy principle) could be used instead of local weak form or additional techniques, for 1D modelling in the present study, two adjacent background cells are connected by a node of the field nodes, and one-piece shape functions for one background cell is adopted [41].

3. Numerical results and discussion

In this section, numerical examples are conducted based on the previously established procedure and formulations. First, the convergence rate and the accuracy of the modelling are investigated. Then, parametric studies are carried out and their numerical results are discussed in detail.

The sandwich beams have three layers as follows: the top ceramic layer made of Silicon nitride (Si_3N_4), the bottom metal layer made of Stainless steel (SUS304), and P-FGM core layer built from Si_3N_4 and SUS304. Material properties, which depend on temperature, are given in Table 1. Poisson's ratio for the core is assumed to be constant and evaluated as the average value of two constituting materials at $T_0 = 300$ K. For LTR and NTR, the temperature change is defined as $\Delta T = T_U - T_L$, ($T_L = T_0 = 300$ K). It should be noted that both temperature dependence (TD) and temperature independence (TID) material properties are considered in this study for comparison. In addition, the beam is assumed to be in a stress-free state at the temperature $T_0 = 300$ K.

For convenience, $\varepsilon_z = 0$ indicates TBT, whereas $\varepsilon_z \neq 0$ indicates quasi-3D theory in the presentations, and non-dimensional quantities are used, as follows, to demonstrate the numerical results.

$$\overline{\omega} = \frac{\omega L^2}{h} \sqrt{\frac{\rho_m}{E_m}}, \qquad \hat{\omega} = \frac{\omega L^2}{h} \sqrt{\frac{12\rho_c}{E_c}}. \qquad (45)$$

E_c in Eq. (45) is estimated at the temperature $T_0 = 300$ K.

The P-FGM sandwich beams with different axially immovable end supports, $u_o(0) = u(L) = 0$, are considered in the investigations. They are simply supported (SS), clamped–clamped (CC), clamped–hinged (CH), and clamped–free (CF).

The PIM-based 1D modelling, which was studied by Chinh et al. [34], showed that nodal distributions have little effect on the accuracy of results. Hence, in this study, uniformly-scattered node is used throughout the analyses for convenience. The scaling factor for determining the size of the influence domains Ω_s is chosen to be 2.0 (3–4 nodes per influence domain in this study). This factor is recommended from 2.0 to 3.0 for mesh-free analyses [40].

3.1. Convergence study

The convergence study is performed for the first natural frequency by increasing the numbers of scattered nodes in the analysis until there is very little change in the solution. The computed results for the tests with different boundary conditions (BCs) are given in Table 2. It can be observed that (1) as the node density increases, the value of the frequency is reduced and converge rapidly; (2) for the same beam theory, the solution of SS boundary condition has the highest convergence rate; (3) TBT ($\varepsilon_z = 0$) converges slightly faster than that of quasi-3D theory ($\varepsilon_z \neq 0$); (4) the 30-node scheme is sufficient to yield reasonably accurate results. This scheme will, therefore, be used throughout the next examples.

Table 2. The convergence of the first natural frequency $\hat{\omega}_1$ of P-FGM sandwich beams
(Type B, $h_c/h_f = 8$, $L/h = 20$, TD, NTR, $k = 0.5$, $\beta = 0.2$, $\Delta T = 50$ K)

BCs	Theory	Number of nodes					
		4	10	20	30	40	50
CF	($\varepsilon_z = 0$)	1.8971	1.8970	1.8969	1.8969	1.8969	1.8969
CF	($\varepsilon_z \neq 0$)	1.6867	1.6666	1.6618	1.6605	1.6599	1.6596
SS	($\varepsilon_z = 0$)	6.4213	6.4203	6.4203	6.4203	6.4203	6.4203
SS	($\varepsilon_z \neq 0$)	6.2914	6.2902	6.2902	6.2902	6.2902	6.2902
CH	($\varepsilon_z = 0$)	10.2134	10.2007	10.1982	10.1974	10.1971	10.1969
CH	($\varepsilon_z \neq 0$)	10.2732	10.1617	10.1406	10.1346	10.1318	10.1302
CC	($\varepsilon_z = 0$)	14.9180	14.8739	14.8639	14.8609	14.8595	14.8586
CC	($\varepsilon_z \neq 0$)	15.3692	14.9546	14.8908	14.8726	14.8641	14.8591

3.2. Verifications

Firstly, the comparative study is for the case of a perfect FGM (Al/Al$_2$O$_3$) sandwich beam working in non-thermal environment by setting both $\beta = 0$ and $\Delta T = 0$. The free vibration of this beam was investigated by Vo et al. [42] using FEM together with both TBT and quasi-3D theory. Material properties are assumed as in [42]. The sandwich beam with the face sheet-core-face sheet thickness ratio of which is 2-1-1 (the thickness of the bottom layer doubles that of the top one) is considered. The values of the first natural frequency are reported in Table 3 and compared with those of Vo et al. [42]. It can be seen that the results obtained from the present study are in excellent agreement with the solution of Vo et al. [42].

Table 3. Comparison of the first non-dimensional frequency $\overline{\omega}_1$ of perfect FGM (Al/Al$_2$O$_3$) sandwich beams ($L/h = 5$, 2-1-1 beams)

BCs	Source	Theory	k				
			0	0.5	1	5	10
CF[a]	Present	$\varepsilon_z = 0$	1.2857	1.2823	1.2820	1.2871	1.2895
	Ref. [42]	$\varepsilon_z = 0$	1.2857	1.2823	1.2819	1.2870	1.2894
	Present	$\varepsilon_z \neq 0$	1.3114	1.3085	1.3081	1.3123	1.3143
	Ref. [42]	$\varepsilon_z \neq 0$	1.3111	1.3082	1.3078	1.3120	1.3140
SS[a]	Present	$\varepsilon_z = 0$	3.4833	3.4570	3.4457	3.4353	3.4361
	Ref. [42]	$\varepsilon_z = 0$	3.4836	3.4573	3.4460	3.4356	3.4364
	Present	$\varepsilon_z \neq 0$	3.5469	3.5222	3.5111	3.4980	3.4975
	Ref. [42]	$\varepsilon_z \neq 0$	3.5478	3.5233	3.5122	3.4993	3.4988
CC	Present	$\varepsilon_z = 0$	7.2331	7.0716	6.9749	6.7493	6.6950
	Ref. [42]	$\varepsilon_z = 0$	7.2279	7.0660	6.9690	6.7424	6.6878
	Present	$\varepsilon_z \neq 0$	7.3867	7.2189	7.1172	6.8759	6.8168
	Ref. [42]	$\varepsilon_z \neq 0$	7.3870	7.2195	7.1178	6.8757	6.8163

[a] denotes the axially movable BC.

The next verification is devoted to the thermal vibration of single layer FGM beams with porosities. P-FGM sandwich beams are modified to be a specific case as single layer P-FGM beams by setting the face sheet thickness to zero (setting $h_3 = h/2$ and $h_2 = -h/2$ in the analysis). The thermal vibration of those beams was conducted by Ebrahimi and Jafari [26] using Navier solution and TBT. FGM of the beams is composed of Si$_3$N$_4$ and SUS304 whose material properties are given in Table 1. In order to be compatible with the study of Ebrahimi and Jafari [26] for the comparison purpose, two conditions are adopted in this analysis: (1) SS beam with axially movable boundary condition is imposed because Ebrahimi and Jafari [26] implemented Navier method for the problem; however, the thermal stress resultant

is supposed to exist ($N^{th} \neq 0$); and (2) $T_L - T_0 = 5$ K for the cases of LTR and NTR. The values of the first frequency are presented in Table 4. An excellent correlation is achieved through the comparison.

Table 4. Comparison of the first non-dimensional frequency $\overline{\omega}_1$ of the single layer P-FGM beams ($L/h = 20$, TD, SS, $\Delta T = 80$ K, $\beta = 0.2$, $\varepsilon_z = 0$)

Sources	Temperature rise	k					
		0	0.1	0.2	1	2	5
Even porosity distribution							
Present	UTR	7.1026	5.7328	4.9591	3.1213	2.6493	2.2937
Ref. [26]		7.1036	5.7336	4.9597	3.1215	2.6493	2.2933
Present	LTR	7.4624	6.1073	5.3428	3.5223	3.0463	2.6851
Ref. [26]		7.4634	6.1080	5.3434	3.5226	3.0463	2.6848
Present	NTR	7.4624	6.1159	5.3552	3.5441	3.0673	2.6998
Ref. [26]		7.4634	6.1128	5.3513	3.5380	3.0612	2.6952
Uneven porosity distribution							
Present	UTR	6.2747	5.3031	4.7033	3.1454	2.7164	2.3821
Ref. [26]		6.2757	5.3038	4.7039	3.1456	2.7163	2.3817
Present	LTR	6.6794	5.7248	5.1352	3.5947	3.1608	2.8206
Ref. [26]		6.6803	5.7254	5.1357	3.5949	3.1608	2.8203
Present	NTR	6.6794	5.7319	5.1456	3.6134	3.1787	2.8329
Ref. [26]		6.6803	5.7304	4.1440	3.6111	3.1764	2.8313

3.3. Parametric studies

After testing the convergency and confirming the accuracy, the next examples are performed to investigate the free vibration characteristics of P-FGM sandwich beams in a thermal environment.

Table 5 presents the first frequency $\hat{\omega}_1$ of P-FGM sandwich beams with both TD and TID material properties under UTR. For TID case, material properties are evaluated at the temperature $T_0 = 300$ K. This table shows that TD solution gives significantly different and lower values when compared to the TID ones. The greater the temperature change ΔT, the greater the difference of the computed values between TD and TID. The main reason is that modulus elastic E is reduced for TD, but constant for TID as the temperature increases. Of course, TD predicts responses of the beams more realistically than TID does. The frequency decreases with the increase of the volume fraction index (k). This is due to the fact that decreasing the ceramic constituent of FGM as k increases makes the beams softer. As expected, due to the compressive force N^{th} that reduces the geometrical stiffness

Table 5. The first non-dimensional frequency $\hat{\omega}_1$ of P-FGM beams with TD and TID material properties under UTR ($L/h = 20$, SS, $\beta = 0.2$, $h_c/h_f = 8$)

TD/TID	ΔT (K)	Theory	Type A (even)			Type B (uneven)		
			k			k		
			0.25	0.5	5	0.25	0.5	5
TD	0	$\varepsilon_z = 0$	7.6851	6.8933	5.1613	7.4867	6.7943	5.2111
		$\varepsilon_z \neq 0^{(*)}$	7.6911	6.8990	5.1656	7.4921	6.7995	5.2150
		$\varepsilon_z \neq 0$	7.6911	6.8990	5.1656	7.4921	6.7995	5.2150
	60	$\varepsilon_z = 0$	6.7192	5.9550	4.3183	6.4260	5.7581	4.2667
		$\varepsilon_z \neq 0^{(*)}$	6.6397	5.8769	4.2454	6.3364	5.6695	4.1829
		$\varepsilon_z \neq 0$	6.3277	5.5692	3.9580	5.9868	5.3228	3.8539
	120	$\varepsilon_z = 0$	5.5197	4.7680	3.1940	5.0717	4.4075	2.9582
		$\varepsilon_z \neq 0^{(*)}$	5.3092	4.5555	2.9788	4.8257	4.1561	2.6934
		$\varepsilon_z \neq 0$	4.4578	3.6767	2.0092	3.7993	3.0731	1.3525
TID	0	$\varepsilon_z = 0$	7.6851	6.8933	5.1613	7.4867	6.7943	5.2111
		$\varepsilon_z \neq 0^{(*)}$	7.6911	6.8990	5.1656	7.4921	6.7995	5.2150
		$\varepsilon_z \neq 0$	7.6911	6.8990	5.1656	7.4921	6.7995	5.2150
	60	$\varepsilon_z = 0$	6.7964	6.0256	4.3749	6.5057	5.8321	4.3279
		$\varepsilon_z \neq 0^{(*)}$	6.7204	5.9511	4.3054	6.4200	5.7475	4.2480
		$\varepsilon_z \neq 0$	6.4215	5.6565	4.0313	6.0855	5.4160	3.9346
	120	$\varepsilon_z = 0$	5.7722	5.0099	3.4119	5.3475	4.6760	3.2104
		$\varepsilon_z \neq 0^{(*)}$	5.5833	4.8201	3.2233	5.1284	4.4536	2.9825
		$\varepsilon_z \neq 0$	4.8288	4.0491	2.4122	4.2351	3.5262	1.9408

$^{(*)}$ $\sigma_{x2}^{th} = 0$

($\mathbf{K}^G$), the values of the frequency decrease with increasing of ΔT. It is seen that when $\Delta T = 0$, the assumptions of $\varepsilon_z \neq 0^{(*)}$, which is not included σ_{x2}^{th} (the axial stress due to the thermal strain in the thickness direction), and of $\varepsilon_z \neq 0$ give the same frequency values, but those values are slightly greater than the values which the assumption of $\varepsilon_z = 0$ gives. However, when $\Delta T \neq 0$, those features are reversed due to the additional effects caused by $N^{th} \neq 0$ (see Eqs. (22)–(24)). The effect of the assumptions is more pronounced with high ΔT. In this situation, the assumption of $\varepsilon_z \neq 0$ gives the smallest values of all because the compressive force N^{th} is the greatest. Besides, in the same analysis conditions, P-FGM beams of Type A give higher frequency values than the ones of Type B do. The reason is that a higher pore density in Type A beams than that in Type B ones reduces the effective mass density (ρ). Thus, the even distribution of porosities is more effective in increasing the frequency than an uneven distribution.

The effects of span-to-height ratio (L/h) and beam theories on the first frequency are plotted in Fig. 3 for Type A beam and in Fig. 4 for Type B beam.
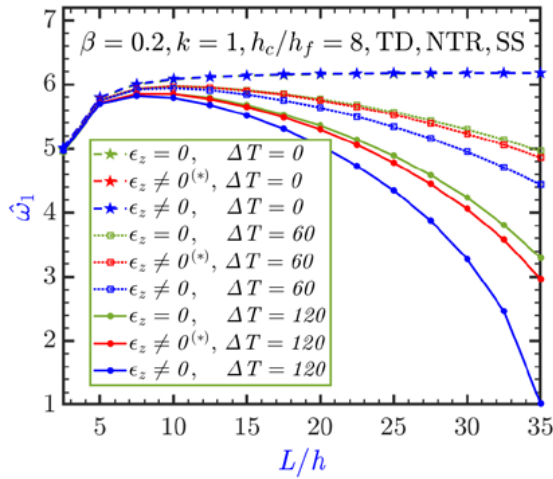
Fig. 3. Variation of the first non-dimensional frequency $\hat{\omega}_1$
of Type A beam with respect to L/h
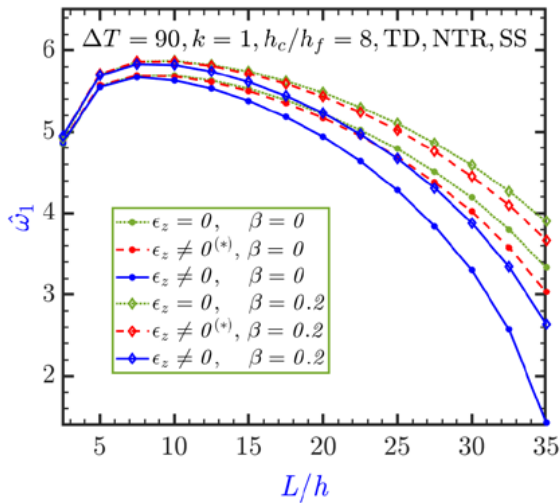
Fig. 4. Variation of the first non-dimensional frequency $\hat{\omega}_1$
of Type B beam with respect to L/h

As can be seen, among the three assumptions ($\varepsilon_z = 0$, $\varepsilon_z \neq 0^{(*)}$, $\varepsilon_z \neq 0$), the assumption $\varepsilon_z \neq 0$ gives the smallest frequency, whereas the greatest one belongs to $\varepsilon_z = 0$. Furthermore, the gaps of the curves among the three assumptions go up with the increase of L/h. From Figs. 3 and 4, one can also observe coupling effects of geometric nonlinearity associated with N^{th} and shear deformation on the frequency. When L/h increases, the shear deformation decreases but the geometric nonlinearity increases. As L/h gradually increases, the frequency increases due to

the major effects of shear deformation but minor effects of the geometric nonlinearity. However, as $L/h > 7.5$, those effect characteristics are in contrast and make the frequency rapidly reducing, especially for $\varepsilon_z \neq 0$ and high ΔT, or $\beta = 0$. It also can be seen clearly in Fig. 3 for the specific case of $\Delta T = 0$ K, there is no effect of the geometric nonlinearity due to $N^{th} = 0$; the frequency is only affected by the shear strain. Therefore, as L/h increases, the slope of the curve increases rapidly, then gradually, and then it remains almost constant.

Variation of the first frequency $\hat{\omega}_1$ with respect to the core-to-face sheet thickness ratio (h_c/h_f) for different values of the volume fraction index (k) is portrayed in Fig. 5. It can be seen that the frequency decreases with the increase of k. Moreover, when $k > 2$, it has little effect on the frequency; the gap between two adjacent curves is rather small. When h_c/h_f increases, the frequency usually increases for small k ($k < 1$), but it can decrease for high values of k.
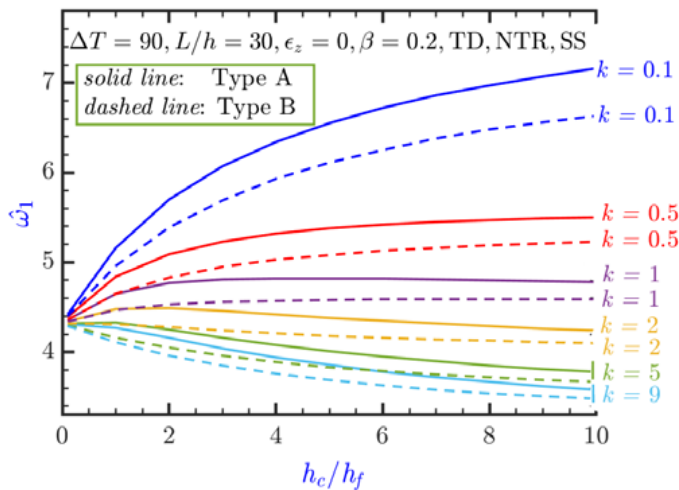
Fig. 5. Variation of the first non-dimensional frequency $\hat{\omega}_1$
of P-FGM with respect to h_c/h_f

The variation of the first frequency $\hat{\omega}_1$ with respect to the temperature change (ΔT) is illustrated in Fig. 6 for different values of the porosity volume fraction (β) and the assumptions of ε_z. It is clear that when the temperature increases, the frequency decreases at a faster and faster rate and finally vanishes at the critical buckling temperature. The gaps between the curves with the same assumption of ε_z but different β increase with the increasing of ΔT. The gaps between the curves with the same β but different assumptions of ε_z also increase with the increasing of ΔT. Another interesting feature is seen that the higher frequency values are obtained for the greater value of β. This shows the effectiveness of porous materials in increasing frequency values.

Fig. 7 has the main purpose to compare the frequency, which is predicted by different types of temperature distribution (UTR, LTR, NTR), with respect to the
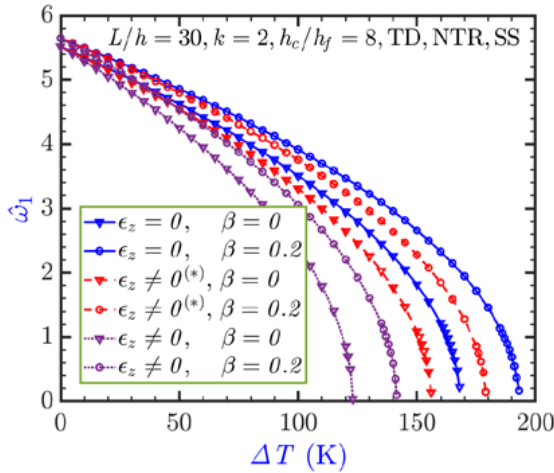
Fig. 6. Variation of the first non-dimensional frequency $\hat{\omega}_1$
of Type B P-FGM with respect to ΔT
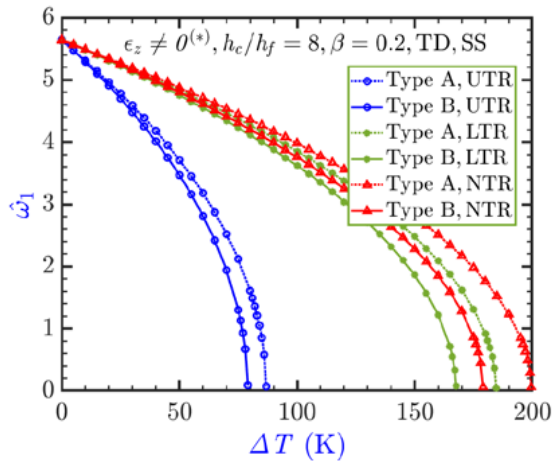
Fig. 7. Variation of $\hat{\omega}_1$ with respect to ΔT for three types
of temperature rise

temperature changes (ΔT). Both Type A beam and Type B beam with $L/h = 30$ and $k = 2$ are considered. As expected, UTR gives the smallest frequency of all because all points in the beam are subjected to ΔT, whereas LTR and NTR, $\Delta T = 0$ at the bottom and varies to ΔT at the top of the beams. It can be observed that for the same beam type and ΔT, NTR gives slightly higher frequency values than LTR does. In addition, the difference of the computed frequency between LTR and NTR for the same beam type increases with the increasing of ΔT; the difference of the computed frequency between Type A and Type B beams for the same temperature rise also increases with the increasing of ΔT.

The effect of BCs on the first frequency $\hat{\omega}_1$ is plotted in Fig. 8 by varying L/h ratio. As expected, the frequency of CC beams is the greatest, followed with CH, SS, and CF beams, respectively. It should be noted that the slope of CC curve in Fig. 8 is larger than that of the other curves in the region of small L/h. It can be explained by the fact that shear deformation has the strongest influence on CC beams when compared to the beams with the other BCs in this region.
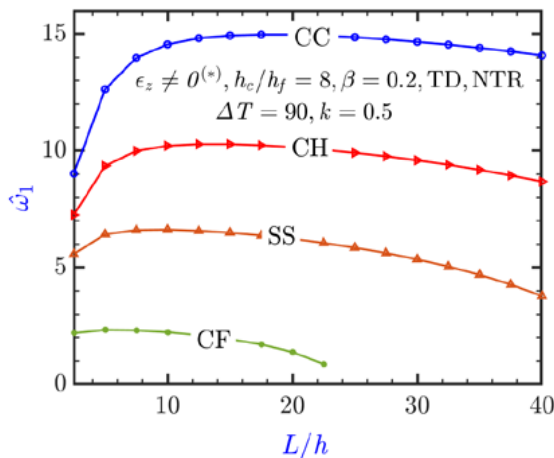
Fig. 8. Variation of $\hat{\omega}_1$ of Type A beam with respect to L/h
for various BCs

4. Summary and conclusions

In this paper, the vibration behavior of sandwich beams with porous FGM core and solid-isotropic face sheets in thermal environment is analyzed and examined. Mesh-free approach based on point interpolation technique and polynomial basis is utilized to approximate four-unknown displacement field for 1D modelling. Third-order beam theory and quasi-3D beam theory with/without thermal stress assumption due to thermal strain in the thickness direction are considered in the analysis. Two types of porosity distribution, even and uneven distributions, and three types of temperature rise, UTR, LTR and NTR, are supposed. The effects of beam theories, porosity distributions, porosity volume fraction, temperature rises, temperature change, span-to-height ratio, different boundary conditions, layer thickness ratio, volume fraction index on the fundamental frequency of the beams are investigated in detail. Major conclusions can be reached from the study:

- The mesh-free approach shows the accuracy and effectiveness in 1D modelling problems. It gives a remarkable solution without needing many scattered nodes;
- The higher the temperature change is, the faster the frequency decreases and vanishes at the critical buckling temperature;

- The discrepancy between the frequencies, which is analyzed by beam assumptions/values of porosity volume fraction/temperature rises, increases with increasing of temperature change, especially when the temperature stays in a region which is closed to the critical buckling temperature;
- The effects of shear deformation and geometric nonlinearity on thermal vibration of the beams through span-to-high ratio (L/h) have two tendencies. When L/h is small, the major effect belongs to the shear strain, the minor effect is for geometric nonlinear. When L/h is large, those features are reversed;
- The nonlinear temperature rise yields a slightly higher frequency than the linear one;
- The increasing value of the porosity volume fraction results in an increase in the frequency;
- Even distribution of porosities is more effective in increasing the frequency than uneven distribution;
- When the core thickness-to-face sheet thickness ratio increases, the frequency increases for small k but it can decrease for large k.

Acknowledgements

References

[1] D.K. Jha, T. Kant, and R.K. Singh. A critical review of recent research on functionally graded plates. *Composite Structures*, 96:833–849, 2013. doi:10.1016/j.compstruct.2012.09.001.

[2] A.S. Sayyad and Y.M. Ghugal. Modeling and analysis of functionally graded sandwich beams: a review. *Mechanics of Advanced Materials and Structures*, 26(21):1776–1795, 2019. doi:10.1080/15376494.2018.1447178.

[3] A. Paul and D. Das. Non-linear thermal post-buckling analysis of FGM Timoshenko beam under non-uniform temperature rise across thickness. *Engineering Science Technology, an International Journal*, 19(3):1608–1625, 2016. doi:10.1016/j.jestch.2016.05.014.

[4] A. Fallah and M.M. Aghdam. Thermo-mechanical buckling and nonlinear free vibration analysis of functionally graded beams on nonlinear elastic foundation. *Composites Part B: Engineering*, 43(3):1523–1530, 2012. doi: 10.1016/j.compositesb.2011.08.041.

[5] A.I. Aria and M.I. Friswell. Computational hygro-thermal vibration and buckling analysis of functionally graded sandwich microbeams. *Composites Part B: Engineering*, 165:785–797, 2019. doi: 10.1016/j.compositesb.2019.02.028.

[6] S.E. Esfahani, Y. Kiani, and M.R. Eslami. Non-linear thermal stability analysis of temperature dependent FGM beams supported on non-linear hardening elastic foundations. *International Journal of Mechanical Sciences*, 69:10–20, 2013. doi: 10.1016/j.ijmecsci.2013.01.007.

[7] M. Lezgy-Nazargah. Fully coupled thermo-mechanical analysis of bi-directional FGM beams using NURBS isogeometric finite element approach. *Aerospace Science and Technology*, 45:154–164, 2015. doi: 10.1016/j.ast.2015.05.006.

[8] L.C. Trinh, T.P. Vo, H.-T. Thai, and T.-K. Nguyen. An analytical method for the vibration and buckling of functionally graded beams under mechanical and thermal loads. *Composites Part B: Engineering*, 100:152–163, 2016. doi: 10.1016/j.compositesb.2016.06.067.

[9] T.-K. Nguyen, B.-D. Nguyen, T.P. Vo, and H.-T. Thai. Hygro-thermal effects on vibration and thermal buckling behaviours of functionally graded beams. *Composite Structures*, 176:1050–1060, 2017. doi: 10.1016/j.compstruct.2017.06.036.

[10] P. Malekzadeh and S. Monajjemzadeh. Dynamic response of functionally graded beams in a thermal environment under a moving load. *Mechanics of Advanced Materials and Structures*, 23(3):248–258, 2016. doi: 10.1080/15376494.2014.949930.

[11] N. Wattanasakulpong, B. Gangadhara Prusty, and D.W. Kelly. Thermal buckling and elastic vibration of third-order shear deformable functionally graded beams. *International Journal of Mechanical Sciences*, 53(9):734–743, 2011. doi: 10.1016/j.ijmecsci.2011.06.005.

[12] S.C. Pradhan and T. Murmu. Thermo-mechanical vibration of FGM sandwich beam under variable elastic foundations using differential quadrature method. *Journal of Sound and Vibration*, 321(1-2):342–362, 2009. doi: 10.1016/j.jsv.2008.09.018.

[13] G.-L. She, F.-G. Yuan, and Y.-R. Ren. Thermal buckling and post-buckling analysis of functionally graded beams based on a general higher-order shear deformation theory. *Applied Mathematical Modelling*, 47:340–357, 2017. doi: 10.1016/j.apm.2017.03.014.

[14] H.-S. Shen and Z.-X. Wang. Nonlinear analysis of shear deformable FGM beams resting on elastic foundations in thermal environments. *International Journal of Mechanical Sciences*, 81:195–206, 2014. doi: 10.1016/j.ijmecsci.2014.02.020.

[15] T.T. Tran, N.H. Nguyen, T.V. Do, P.V. Minh, and N.D. Duc. Bending and thermal buckling of unsymmetric functionally graded sandwich beams in high-temperature environment based on a new third-order shear deformation theory. *Journal of Sandwich Structures & Materials*, 23(3):906–930, 2021. doi: 10.1177/1099636219849268.

[16] A.R. Setoodeh, M. Ghorbanzadeh, and P. Malekzadeh. A two-dimensional free vibration analysis of functionally graded sandwich beams under thermal environment. *Proceedings of the Institution of Mechanical Engineers, Part C: Journal of Mechanical Engineering Science*, 226(12):2860–2873, 2012. doi: 10.1177/0954406212440669.

[17] L. Chu, G. Dui, and Y. Zheng. Thermally induced nonlinear dynamic analysis of temperature-dependent functionally graded flexoelectric nanobeams based on nonlocal simplified strain gradient elasticity theory. *European Journal of Mechanics - A/Solids*, 82:103999, 2020. doi: 10.1016/j.euromechsol.2020.103999.

[18] Y. Fu, J. Wang, and Y. Mao. Nonlinear analysis of buckling, free vibration and dynamic stability for the piezoelectric functionally graded beams in thermal environment. *Applied Mathematical Modelling*, 36(9):4324–4340, 2012. doi: 10.1016/j.apm.2011.11.059.

[19] W.-R. Chen, C.-S. Chen, and H. Chang. Thermal buckling analysis of functionally graded Euler-Bernoulli beams with temperature-dependent properties. *Journal of Applied and Computational Mechanics*, 6(3):457–470, 2020. doi: 10.22055/JACM.2019.30449.1734.

[20] N. Wattanasakulpong and V. Ungbhakorn. Linear and nonlinear vibration analysis of elastically restrained ends FGM beams with porosities. *Aerospace Science and Technology*, 32(1):111–120, 2014. doi: 10.1016/j.ast.2013.12.002.

[21] N. Wattanasakulpong and A. Chaikittiratana. Flexural vibration of imperfect functionally graded beams based on Timoshenko beam theory: Chebyshev collocation method. *Meccanica*, 50(5):1331–1342, 2015. doi: 10.1007/s11012-014-0094-8.

[22] D. Shahsavari, M. Shahsavari, L. Li, and B. Karami. A novel quasi-3D hyperbolic theory for free vibration of FG plates with porosities resting on Winkler/Pasternak/Kerr foundation. *Aerospace Science and Technology*, 72:134–149, 2018. doi: 10.1016/j.ast.2017.11.004.

[23] Z. Ibnorachid, L. Boutahar, K. EL Bikri, and R. Benamar. Buckling temperature and natural frequencies of thick porous functionally graded beams resting on elastic foundation in a thermal environment. *Advances in Acoustics and Vibration*, 2019:7986569, 2019. doi: 10.1155/2019/7986569.

[24] Ş.D. Akbaş. Thermal effects on the vibration of functionally graded deep beams with porosity. *International Journal of Applied Mechanics*, 9(5):1750076, 2017. doi: 10.1142/S1758825117500764.

[25] H. Babaei, M.R. Eslami, and A.R. Khorshidvand. Thermal buckling and postbuckling responses of geometrically imperfect FG porous beams based on physical neutral plane. *Journal of Thermal Stresses*, 43(1):109–131, 2020. doi: 10.1080/01495739.2019.1660600.

[26] F. Ebrahimi and A. Jafari. A higher-order thermomechanical vibration analysis of temperature-dependent FGM beams with porosities. *Journal of Engineering*, 2016:9561504, 2016. doi: 10.1155/2016/9561504.

[27] Y. Liu, S. Su, H. Huang, and Y. Liang. Thermal-mechanical coupling buckling analysis of porous functionally graded sandwich beams based on physical neutral plane. *Composites Part B: Engineering*, 168:236–242, 2019. doi: 10.1016/j.compositesb.2018.12.063.

[28] S.S. Mirjavadi, A. Matin, N. Shafiei, S. Rabby, and B. Mohasel Afshari. Thermal buckling behavior of two-dimensional imperfect functionally graded microscale-tapered porous beam. *Journal of Thermal Stresses*, 40(10):1201–1214, 2017. doi: 10.1080/01495739.2017.1332962.

[29] E. Salari, S.A. Sadough Vanini, A.R. Ashoori, and A.H. Akbarzadeh. Nonlinear thermal behavior of shear deformable FG porous nanobeams with geometrical imperfection: Snap-through and postbuckling analysis. *International Journal of Mechanical Sciences*, 178:105615, 2020. doi: 10.1016/j.ijmecsci.2020.105615.

[30] N. Ziane, S.A. Meftah, G. Ruta, and A. Tounsi. Thermal effects on the instabilities of porous FGM box beams. *Engineering Structures*, 134:150–158, 2017. doi: 10.1016/j.engstruct.2016.12.039.

[31] A.I. Aria, T. Rabczuk, and M.I. Friswell. A finite element model for the thermo-elastic analysis of functionally graded porous nanobeams. *European Journal of Mechanics - A/Solids*, 77:103767, 2019. doi: 10.1016/j.euromechsol.2019.04.002.

[32] G.R. Liu and Y.T. Gu. A point interpolation method for two-dimensional solids. *International Journal for Numerical Methods in Engineering*, 50(4):937–951, 2001. doi: 10.1002/1097-0207(20010210)50:4<937::AID-NME62>3.0.CO;2-X.

[33] Y.T. Gu and G.R. Liu. A local point interpolation method for static and dynamic analysis of thin beams. *Computer Methods in Applied Mechanics and Engineering*, 190(42):5515–5528, 2001. doi: 10.1016/S0045-7825(01)00180-3.

[34] T.H. Chinh, T.M. Tu, D.M. Duc, and T.Q. Hung. Static flexural analysis of sandwich beam with functionally graded face sheets and porous core via point interpolation meshfree method based on polynomial basic function. *Archive of Applied Mechanics*, 91:933–947, 2021. doi: 10.1007/s00419-020-01797-x.

[35] J.N. Reddy and C.D. Chin. Thermomechanical analysis of functionally graded cylinders and plates. *Journal of Thermal Stresses*, 21(6):593–626, 1998. doi: 10.1080/01495739808956165.

[36] H.-S. Shen. *Functionally Graded Materials: Nonlinear Analysis of Plates and Shells*. CRC Press, 2016. doi: 10.1201/9781420092578.

[37] T.-K. Nguyen, T.P. Vo, B.-D. Nguyen, and J. Lee. An analytical solution for buckling and vibration analysis of functionally graded sandwich beams using a quasi-3D shear deformation theory. *Composite Structures*, 156:238–252, 2016. doi: 10.1016/j.compstruct.2015.11.074.

[38] M. Şimşek. Fundamental frequency analysis of functionally graded beams by using different higher-order beam theories. *Nuclear Engineering and Design*, 240(4):697–705, 2010. doi: 10.1016/j.nucengdes.2009.12.013.

[39] J.N. Reddy. *Mechanics of Laminated Composite Plates and Shells: Theory and Analysis*, 2nd ed. CRC Press, 2003.

[40] G.R. Liu. *Meshfree Methods: Moving Beyond the Finite Element Method*. 2nd ed. Taylor & Francis, 2009. doi: 10.1201/9781420082104.

[41] G.R. Liu, Y.T. Gu, and K.Y. Dai. Assessment and applications of point interpolation methods for computational mechanics. *International Journal for Numerical Methods in Engineering*, 59(10):1373–1397, 2004. doi: 10.1002/nme.925.

[42] T.P. Vo, H.-T. Thai, T.-K. Nguyen, F. Inam, and J. Lee. A quasi-3D theory for vibration and buckling of functionally graded sandwich beams. *Composite Structures*, 119:1–12, 2015. doi: 10.1016/j.compstruct.2014.08.006.